Materials Science & Engineering A 890 (2024) 145903

Contents lists available at ScienceDirect

Materials Science & Engineering A

journal homepage: www.elsevier.com/locate/msea

# Deformation behavior of TiB reinforced Ti and Ti6Al4V composite particles under in-situ microcompression

Bo Li [a,b,*], Deng Pan [a,e], Xin Zhang [a,b], Lei Liu [a], Lina Gao [a], Shaolong Li [a], Yuanbin Qin [c], Yabo Fu [d], Shufeng Li [a,b,**]

[a] School of Materials Science and Engineering, Xi'an University of Technology, Xi'an, 710048, China
[b] Xi'an Key Laboratory of Advanced Powder Metallurgy Materials and New Technology, Xi'an University of Technology, Xi'an, 710048, China
[c] State Key Laboratory for Mechanical Behavior of Materials, School of Materials Science and Engineering, Xi'an Jiaotong University, Xi'an 710049, China
[d] Zhejiang Provincial Key Laboratory for Cutting Tools, Taizhou University, Jiaojiang 318000, Zhejiang, China
[e] Xi'an Sailong Additive Technology Co., Ltd., Xi'an 710018, China

ARTICLE INFO

*Keywords:*
Titanium matrix composites
Microcompression
Particles
Plastic deformation
Strain hardening

ABSTRACT

To reveal the role of nano-TiB whiskers in micromechanical behaviors of two common titanium composite particles (TCPs), this paper presents experimental investigation on the elastic and plastic deformation of micron-sized Ti-TiBw and Ti6Al4V-TiBw particles. Scanning electron microscope with in-situ uniaxial compression experiment of single TCP was performed within a diameter range of ~1–5 μm. This study enables detailed insights into the elastic and plastic deformation and geometrical shape evolution of TiBw reinforced TCPs. It is found that, when the particle size decreases, the flow stress and contact yield stress in microcompression for both TCPs exceed the yield strength of bulk composite pillars with identical content of TiB. The contact yield stress is as high as ~1.5 GPa and ~1.3 GPa for the smallest Ti-TiBw (D~1.45 μm) and Ti6Al4V-TiBw (D~1.78 μm) particles measured, respectively. In elastic-plastic and fully plastic regime, the steady plastic flow for both particles can be maintained over ~2 GPa till the engineering compressive strain of $\varepsilon_E \sim$ -0.4. Compared with bulk composites, higher strain hardening rate of ~34.2 and ~37.5 GPa for Ti-TiBw and Ti6Al4V-TiBw particles demonstrate remarkable pinning capacity induced by nano-TiBw network. No structural damage and microcracks was observed in surface morphology of severely deformed Ti6Al4V-TiBw particles, showing distinctive microscale plasticity. The deformation and strain hardening mechanism for such composite particles have been discussed in terms of grain size, aspect ratio of TiBw and the network architecture.

## 1. Introduction

Metallic composite particles (MCPs) are one effective strategy not only to solve the strength-ductility dilemma in metallic composites, but also to enhance the fracture and fatigue resistance of metallic materials in the fields of advanced powder metallurgy and additive manufacturing [1–8]. So far, the preparation of spherical MCPs have been realized in many matrices, such as Ti [3,5], Ti6Al4V (Ti64) [2], Al [6], AlSi10Mg [7,8], and Cu [9]. The MCPs itself can be also regarded as a miniaturized composite system combined with both in-situ grown nano-ceramic reinforcements and fine grains in matrix because of the rapid solidification process during gas atomization [3,5]. With the in-depth understanding of the relationship between the intrinsic/extrinsic size and mechanical property in various metals at small length scales, the emergence of MCPs provides us good opportunity to probe the micromechanical responses of various composite systems at similar size level. In previous literature, numerous experimental and theoretical studies on compression of micro/nano-scale particles and spheres, e.g., metals [10–14], ceramics [15,16], semiconductors [17,18], and even polymers [19], have been performed not only to provide mechanical properties of small-sized spherical solids, but also to reveal plastic flow behavior, size-dependent effect and strain hardening capacity [20–24]. However, the knowledge on the deformation behavior of MCPs is still rare, partly because of the fabrication difficulty of high-end spherical MCPs relative to metallic powders. Different from metals and alloys, the strengthening and hardening of metallic composites reinforced by ceramic phases

* Corresponding authorSchool of Materials Science and Engineering, Xi'an University of Technology, Xi'an, 710048, China.
** Corresponding authorSchool of Materials Science and Engineering, Xi'an University of Technology, Xi'an, 710048, China.
*E-mail addresses:* libo930@xaut.edu.cn (B. Li), shufengli@xaut.edu.cn (S. Li).

https://doi.org/10.1016/j.msea.2023.145903
Received 13 September 2023; Received in revised form 30 October 2023; Accepted 9 November 2023
Available online 15 November 2023

derives from a combination of intrinsic property of metallic matrix and the load transfer effect and pinning capacity of reinforcements. As revealed by our recent report, the presence of nano-TiBw network will significantly enhance the critical pressure of martensitic transformation in Ti-TiBw particles upon uniaxial loading, showing higher structural stability against pressure-induced deviatoric stress [25]. Therefore, the experimental research on the role of nano-ceramic reinforcements and their spatial architectures in the deformation behavior of MCPs has tremendous scientific and technological interest.

Titanium matrix composites (TMCs) as one of the most promising structural materials in aerospace and other lightweight engineering applications, have been widely studied in recent decades [26]. Among various ceramic reinforcements, e.g., SiC, TiC, $Al_2O_3$ and $Si_3N_4$, titanium boride (TiB) shows particular advantages of high physical and crystal compatibility of Ti and TiB in addition to high elastic modulus and hardness as an in-situ grown ceramic phase [27]. Furthermore, the experimental and theoretical studies on the role of TiB also displays a broad applicability in enhancing mechanical properties for various metallic composites, e.g., copper matrix composites [28–31]. The in-situ TiB whiskers (TiBw) usually display a near hexagonal shape in cross section and the interfaces between in-situ TiBw and Ti matrix are clean and faceted along the (100) plane of TiB [2,32]. As a brittle and hard phase, the aspect ratio of TiBw was found to be critical for the mechanical properties of TMCs, and the nano-TiBw with larger aspect ratio is beneficial for the enhancement of mechanical property [33,34]. However, the size of TiBw can be rapidly increased with the sintering temperature increase, leading to the coarsening of TiBw during fabrication and interfacial cracking upon mechanical loading. For titanium composite particles (TCPs), the gas atomization process allows the retention of in-situ grown nano-sized TiBw and the size of TiBw usually falls within a few tens of nanometer and its aspect ratio is more than 30 [2,3]. Therefore, it also motivates us to explore the micromechanical performance of TCPs which simultaneously has abovementioned structural characteristics. In addition, different from FCC and BCC metals, the micromechanical behaviors of HCP metals, such as Ti and Mg, are demonstrated to be more complex by pillar compression due to less slip systems [21,22]. So far, previous works focused mostly on the intrinsic size effect in bulk composites, that is, the grain refinement strengthening of the matrix (Hall-Petch mechanism), and/or the size-dependent strengthening of reinforcements (Orowan mechanism, load transfer effect) [2,3,33]. When TMC specimens become small down to micron size and below, there lacks an understanding on the extrinsic sample size effect, and possible dislocation mechanism is still uncertain. The result from microcompression of TCPs is a desirable alternative to study extrinsic size effect on mechanical behavior of small-sized TMC system since surface damage and defects are probably introduced by making micropillar using focused ion beam (FIB) technique.

In the following, two common TCPs, namely, nano-TiBw reinforced Ti and Ti6Al4V composite (Ti-TiBw and Ti64-TiBw) particles with sizes of 1–5 μm, were chosen in the present study because of perfectly spherical shape, well-defined nano-TiBw network and high structural compatibility between TiB and Ti [32,35,36]. In microcompression section, the flow behaviors of both TCPs subjected to uniaxial compression were investigated upon severe plastic deformation. We particularly focused on the elastic and yielding behaviors, and strain-hardening of these TCPs relative to commercial pure Ti (CP–Ti).

## 2. Experimental methods

### 2.1. Fabrication of TCPs

Highly spherical Ti-3.4 vol%TiBw, Ti64-5.1 vol%TiBw and CP-Ti particles were prepared by electrode induction gas atomization (EIGA) method [2,3]. The preparation procedure includes the following steps: 2 wt% $TiB_2$ (3.4 vol% TiBw) and CP-Ti raw powders were mixed by ball milling with a proper ratio, then being compressed into a green compact with 300 × 60 × 60 $mm^3$ by a hydraulic machine (300-ton). Second, the green compact was smelted 2 times into an ingot through the vacuum arc re-melting process, followed by forging process at 1050–1100 °C and machining into a cylindrical bar with φ 45 × 500 mm, which was used as EIGA anode to produce spherical powders. Finally, ultrafine composite powders were sieved into a range of 1–45 μm, as shown in Fig. 1a. Similarly, the Ti64-TiBw powders with a TiB content of 5.1 vol% was fabricated by above procedures. The bulk TMCs with identical volume fraction of TiB were sintered using above Ti-TiBw and Ti64-TiBw powders by spark plasma sintering (SPS). With two heating rates of 100 and 50 °C/min before and after 600 °C, the samples are eventually heated up to 1000 °C followed with a temperature holding of 30 min.

### 2.2. Structural characterization

Microstructural observations and phase analysis of both TMC particles were conducted by a scanning electron microscopy (SEM, JSM-6700F, JEOL) and a transmission electron microscope (TEM, JEM-2010, JEOL). The grain size of matrix and the aspect ratio of TiBw in those particles are statistically determined by SEM characterization. Specifically, the aspect ratio of nano-TiBw is obtained by counting over ~100 whiskers that showing a complete appearance.

### 2.3. In situ microcompression experiments

Single TMC particle is uniaxially compressed between two flat surfaces, that is, a diamond flat punch with a diameter of ~6 μm and a commercial (100) silicon wafer, in a FIB/SEM workstation (Helios 600 Nanolab). The as-made powders were dispersed with anhydrous ethanol and the diluted suspensions were dripped on the silicon substrate by a dip-coating procedure, followed by drying under ambient conditions. The vacuum pumping procedure is operated before compression for at least 30min for the specimen inside the vacuum chamber of SEM. The applied load and deformation obtained by such micromechanical device (Hysitron PI 85L SEM PicoIndenter, Bruker) can make sure at a high resolution of<0.4 μN and<1 nm, respectively. The reliability of this SEM-supported micromechanical device was proven previously [17]. The qualified particles are randomly selected based on the criteria of high sphericity, suitable size and no interference of manipulation (Fig. 1d and e). Then, it is continuously compressed up to a maximum load followed by an unloading. During compression the load and the deformation (the displacement along the loading axis) were synchronously recorded. The loading rate is controlled by a displacement mode of 10 nm/s and the maximum applied load of our device is about 16 mN. The low loading rate enables the application of quasistatic compression so that the frictional effect and rate dependence can be neglected at least in elastic and elastic-plastic regimes.

The bulk reference samples for compression tests were machined in a cylinder shape from as-sintered composites with a size of φ 4 mm × 6 mm and φ 7 mm × 7 mm for Ti-TiBw and Ti64-TiBw, respectively. Bulk compression tests were conducted with a standard static loading by an electronic universal testing machine (DNS 100, Sinotest Equipment Co., Ltd.).

## 3. Results

### 3.1. Structural characterization of Ti-TiBw and Ti64-TiBw particles

Fig. 1a presents the SEM morphology of as-prepared Ti-TiBw particles which display clean surface and high sphericity over 0.9 for almost all particles, and the satellite particles are rare. Similar geometrical morphology was also observed in Ti64-TiBw particles. The schematic of structural model of a single TCP embedded with the discontinuous network of TiBw is illustrated in the inset of Fig. 1a. Fig. 1b–c displays the cross-sectional microstructures of Ti-TiBw and Ti64-TiBw particles, respectively, both of which exhibit the discontinuous networks of

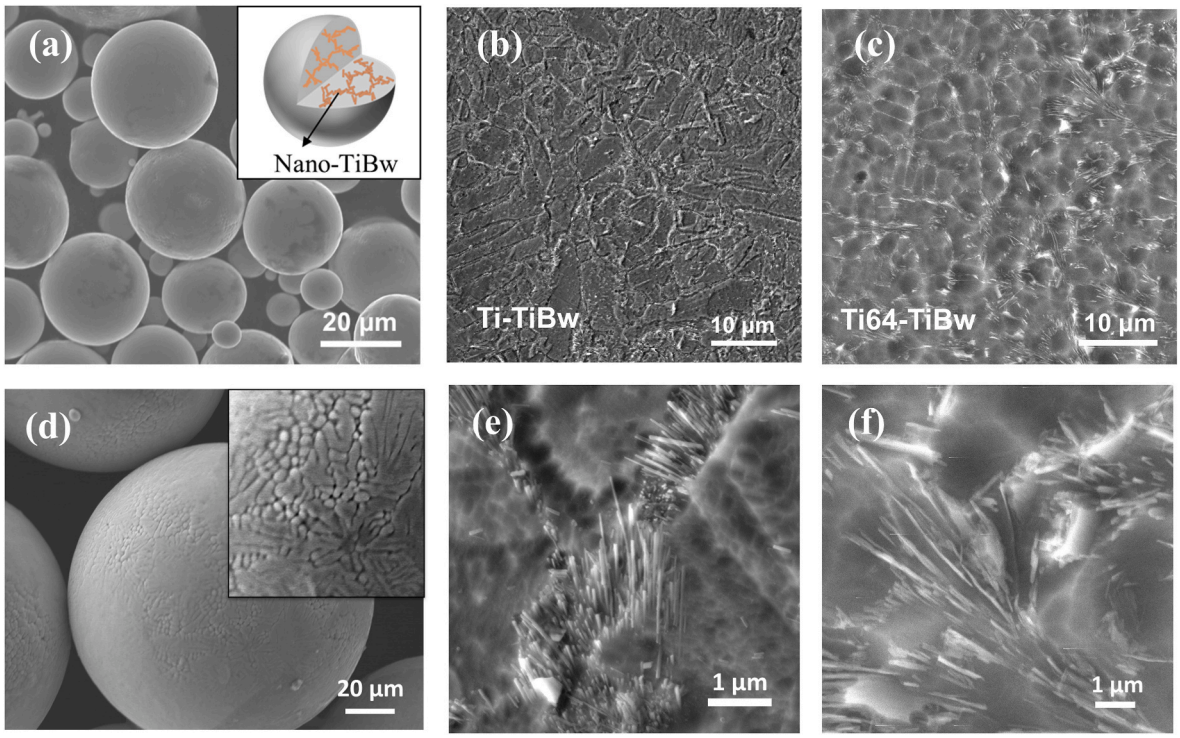


**Fig. 1.** Microstructures of Ti-TiBw and Ti64-TiBw particles. (a) SEM morphology of spherical Ti-TiBw particles. The inset shows a schematic of a TCP model embedded with discontinuous TiBw network. (b, c) Cross-sectional microstructures of a single Ti-TiBw and Ti64-TiBw particle, respectively. (d) Surface morphology of Ti-TiBw particles. (e, f) Detailed microstructures of nano-TiBw aggregated along grain boundaries in (e) Ti-TiBw and (f) Ti64-TiBw particles.

ultrafine nano-TiBw inside the particles. Due to the rapid solidification during gas atomization process, the main phase of α-Ti contains a portion of acicular α" martensites, and the network of nano-TiBw distributes along the grain boundaries (GBs) of the matrix [5]. In Ti64-TiBw particles, typical equiaxed α+β microstructure is found with a characteristic of nano-TiBw network along the GBs of primary β phases [2]. The surface morphology of a Ti-TiBw particle indicates that the surface roughness can be negligible during contact deformation (Fig. 1d). A magnified view of nano-TiBw network in both TCP particles displays an aggregation manner that having a similar orientation, and a high aspect ratio for those whiskers can be easily observed (Fig. 1e and f). With the increase of cooling rate of gas atomization, namely, particle size decreases, the refinement effect is more remarkable for both matrix's grains and the aspect ratio of TiBw. By a statistical analysis based on SEM images, the average aspect ratio of nano-TiBw in present cases could achieve ~42 in Ti-TiBw and ~30 in Ti64-TiBw, respectively, which is close to the results reported by Koo et al. [33]. In contrast, the diameter of TiBw in bulk Ti-TiBw composites sintered by SPS at 1000 °C is within the range of several hundred nanometers to micron-scale [37]. The coarsening of TiBw will lead to the decrease of mechanical property of such sintered composites.

### 3.2. Deformation behaviors of Ti-TiBw and Ti64-TiBw particles

Fig. 2a–d exhibits the representative load-displacement (*F-h*) curves of Ti-TiBw, Ti64-TiBw and CP-Ti particles within 1–5 μm in diameter, respectively. For comparison, the engineering stress and strain curves for bulk Ti-TiBw and Ti64-TiBw composites upon pillar compression are presented in Fig. 2e and f. It is clear that the bulk Ti-TiBw pillar deformed continuously to a large strain of $\varepsilon_E \sim$ -0.5 and shows a typical strain-hardening behavior in plastic regime. The compressive yield strength ($\sigma_{cy}$) defined as the proof stress at $\varepsilon_E = -0.2\%$ is about ~505 MPa for Ti-TiBw pillar, while a larger $\sigma_{cy}$ of ~1058 MPa for Ti64-TiBw pillar. For the latter, macroscopic cracks occur instantly at an angle of 45° relative to the loading axis within a small strain ($\varepsilon_E$<-0.28), showing poor strain-hardening capacity. Let's return to the particles, all samples were subjected to the load limit, and neither structural collapse nor strain burst event was found. As shown in Fig. 2a and b, a significantly enhanced load is observed at severe plastic deformation, implying more pronounced friction between severely compressed sample and diamond indenter, as well as geometrical shape effect, which are commonly seen in particle compression [10,13]. Therefore, the deformation behaviors of these stressed TCPs in elastic and elastoplastic regimes will be elaborated, and the mechanical response related to friction and geometry effect during severe plastic deformation are not discussed here.

Analysis of elastic deformation and yielding of a sphere upon compression is not straightforward relative to pillar compression due to geometric constraints and strain gradients. Unlike a pillar, a compressed sphere will first deform elastically in a very small contact area. At the yield point, local volume near the center of the contact area perpendicular to the loading axis will plastically deform at so-called elastic-plastic loading (EPL) regime [15]. It is restricted to a small volume and the surrounding material still behaves elastically. At a larger strain, the fully plastic mode of deformation is reached and the resultant bulge is approximate to a pillar. For ductile isotropic solids in elastic line contact with non-adhesive point, Hertzian theory is usually used for the prediction of elastic property of a sphere in the half-space approximation. The reduced Young's modulus of the single contact between a sphere and a flat plane, $E^*$, is given by:

$$E^* = \left(\frac{1-\nu_1^2}{E_1} + \frac{1-\nu_2^2}{E_2}\right)^{-1} \quad (1)$$

where $E$ is the Young's modulus and $\nu$ the Poisson's ratio of a sphere and a flat plane. Thus, other quantities for Hertzian contact can be defined by $E^*$:

$$\delta = \left(3F/4E^*\sqrt{R}\right)^{2/3} \quad (2)$$

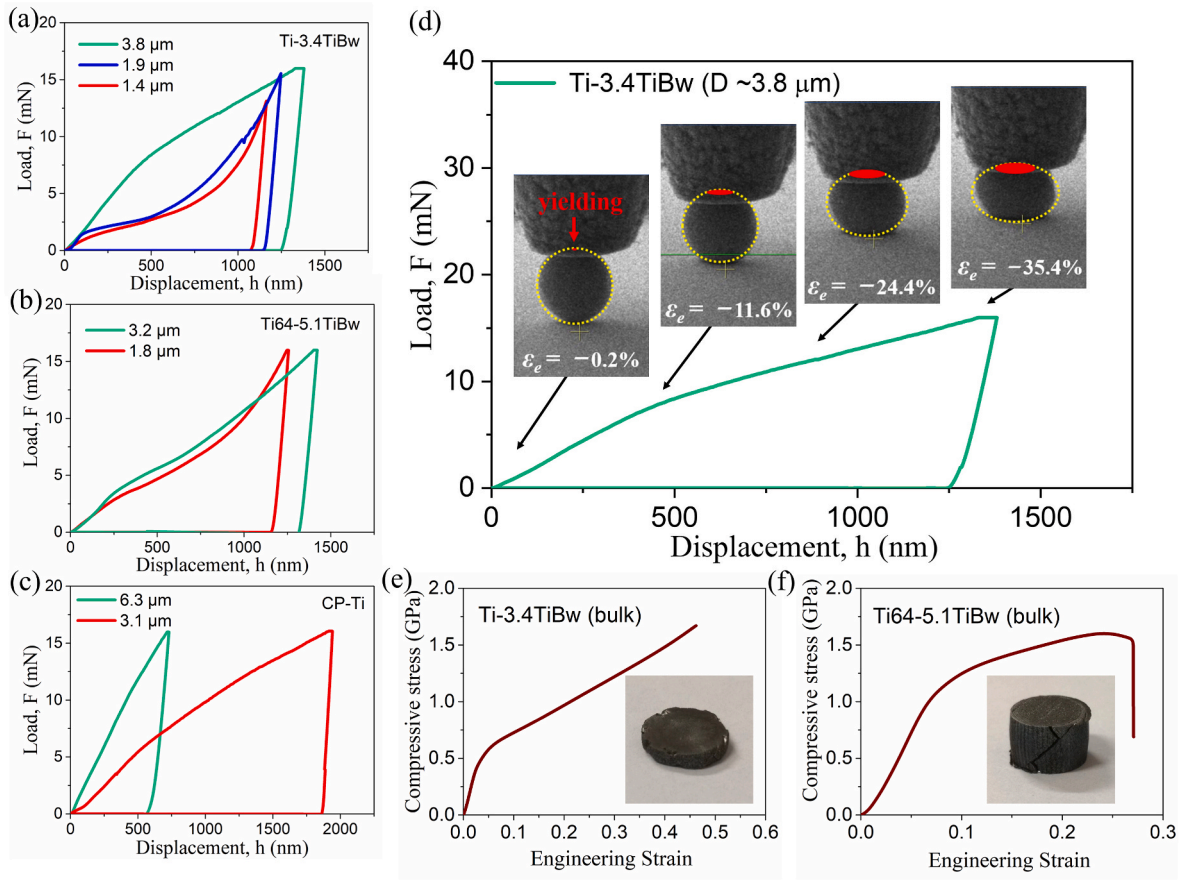


**Fig. 2.** Representative load-displacement curves of (a) Ti-TiBw, (b) Ti64-TiBw and (c) CP-Ti particles upon microcompression. (d) Geometrical shape evolution of a single Ti-TiBw particle from elastic to global plastic deformation. The oval area (red) and the dashed circle (yellow) indicates the calculated contact area and the outline of a stressed particle, respectively. (e, f) Compressive engineering stress-engineering strain curves of bulk Ti-TiBw and Ti64-TiBw composites and the failure and damage after severe plastic deformation (insets). (For interpretation of the references to colour in this figure legend, the reader is referred to the Web version of this article.)

$$a = \sqrt{R\delta} = (3RF/4E^*)^{1/3} \tag{3}$$

$$p_0 = \left(2E^*\sqrt{\delta/R}\right) \Big/ \pi \tag{4}$$

where $\delta$ is the deformation of a sphere and a flat plane, $a$ the contact radius, $R$ the sphere radius, $F$ the applied load in normal direction, $p_0$ the maximum contact pressure. Different from two similar contacts, the use of a diamond flat punch ($E$ = 1143 GPa, $\nu$ = 0.07 [38]) and a silicon substrate ($E$ = 130 GPa, $\nu$ = 0.22 [39]) leads to dissimilar contact deformation. Thus, the $E^*$ for each single contact can be obtained when the elastic modulus of TCPs is known. According to the Hashin-Shtrikman (H–S) theorem, the upper and lower bounds of Young's modulus for a given isotropic two-phase composite can be well predicted [40,41]. Taking the respective $E$ value of 100, 112, and 482 GPa for Ti, Ti64 and TiB, the TiBw volume fraction of 3.4 and 5.1 vol% for Ti and Ti64 composite particles results in a mean value of $E_{\text{Ti-TiBw}}$ and $E_{\text{Ti64-TiBw}}$ of ~106 and ~122 GPa, respectively [40]. The Poisson's ratio for TCPs can be reasonably estimated to be 0.32 [40,42]. Accordingly, the $E^*_{Ti64-TiBw}$, $E^*_{Ti-TiBw}$ and $E^*_{CP-Ti}$ is calculated to be 121.5, 107.1 and 102.2 GPa for the sample-diamond contact, and 68.1, 63.3 and 61.6 GPa for the sample-silicon contact by Eq. (1). If the sample is mounted between two identical plates, the effective reduced Young's modulus ($E^*$ *1/2*) of sample is determined by the half of above two sample-plate contact moduli. However, the dissimilar contacts in our cases yields discrepancy of the actual effective reduced Young's modulus ($E^*$ *eff*) as shown in Fig. 3. To account for dissimilar single contact deformation in total deformation, for example, diamond-tip-sided deformation is

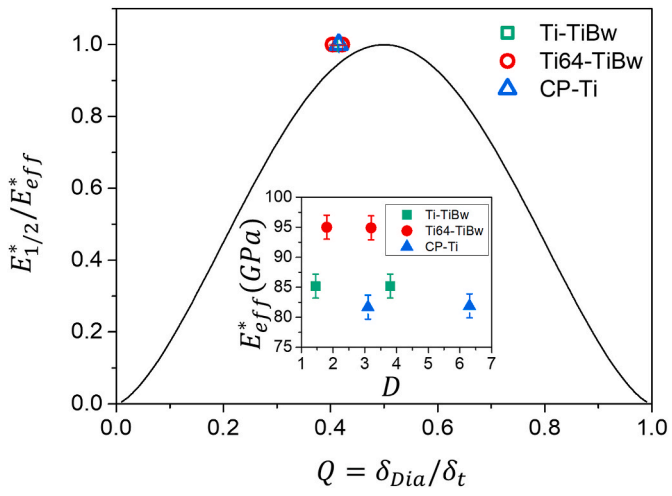


**Fig. 3.** Discrepancy of the ratio of effective reduced Young's modulus of two similar ($E^*_{1/2} = \frac{3}{4}\frac{F}{\sqrt{R}}(2/\delta_t)^{3/2}$) and dissimilar ($E^*_{eff} = \frac{3}{4}\frac{F}{\sqrt{R}}\left(\frac{1}{2\delta_1^{3/2}} + \frac{1}{2\delta_2^{3/2}}\right)$) contacts to theoretical results (solid line) for TCPs and CP-Ti particles as a function of $Q$, which is defined as the fraction of diamond-tip-sided deformation ($\delta_{Dia}$) relative to overall deformation ($\delta_t$). Inset: the actual $E^*_{eff}$ calculated for the TCPs and CP-Ti particles with different sizes.

separately considered by additional quantity of *Q*. The observed discrepancy of the corresponding $E^*$ *1/2/*$E^*$ *eff* for dissimilar contacts agrees well with the claim by Peukert et al. [15]. The calculated $E^*$ *eff* for TCPs and CP-Ti particles is further shown in the inset of Fig. 3. It is found that the $E^*$ *eff* for those particles is lower than that of bulk materials. The reason may stem from the overestimation of single contact deformation calculated by Eq. (2) relative to actual recorded deformation.

In elastic-plastic and fully plastic regimes as shown in Fig. 2, all *F-h* curves progress smoothly and no discontinuity is observed, displaying a typical flow deformation without the formation of cracks or structural collapse. The results of SEM imaging also support this claim. The adhesion of sample and indenter was observed due to friction effect in particular cases when severe plastic deformation is conducted ($\varepsilon_E$>0.5) [13]. To quantitatively analyze the stress during compression, two types of compressive stresses are usually used, i.e., contact pressure ($\sigma_{cont}$) [43] and engineering stress ($\sigma_E$) [13,14]. The engineering stress $\sigma_E$ and strain $\varepsilon_E$ for a sphere can be simply calculated by: $\sigma_E = F/\pi R^2$, and $\varepsilon_E = h/2R$, while $\sigma_{cont} = F_i/A_i$, where $F_i$ is the instantaneous load and $A_i$ is instantaneous contact area that can be determined from the recorded videos.

In general, the onset of yielding of a ductile material can be determined for engineering or mechanics purposes. Here, the Tresca criterion is preferred due to its simple form of $\sigma_y = 2\tau_{max} = max\{|\sigma_1 - \sigma_2|, |\sigma_2 - \sigma_3|, |\sigma_3 - \sigma_1|\}$. A prerequisite to predict the yield strength by either Tresca or von Mises criteria is to calculate three principal stresses ($\sigma_1$,$\sigma_2$, $\sigma_3$). In Hertzian theory, the principal stress at any point of a solid sphere can be depicted using cylindrical coordinates ($\sigma_z, \sigma_r, \sigma_\theta$), and the shear stress $\tau$ is written [15]:

$$\tau = \frac{1}{2}(\sigma_z - \sigma_r) = \frac{p_0}{2}\left\{\frac{3}{2}\frac{a^2}{z^2+a^2} - (1+\nu)\left[1 - \frac{a}{z}\tan^{-1}\left(\frac{a}{z}\right)\right]\right\} \quad (5)$$

Then the curve of the shear stress derived by Eq. (5) for the TCPs ($\nu$ = 0.32) is plotted in Fig. 4a. Obviously, all principal stresses and the shear stress evolve as the deformation along the loading axis under Hertzian pressure. The maximum shear stress located in a depth of $z = 0.49a$ yields $\tau_{max} = 0.31p_0$, thus the first yield point can be predicted to be $\sigma_y = 0.62p_0$. According to the Tresca criterion and Eq. (4), the first yield points for the Ti-TiBw, Ti64-TiBw and CP-Ti particles with different sizes fall within ~1.90–2.41, ~2.07–2.32 and ~1.56–1.75 GPa, respectively (Fig. 4d). Keep in mind that the first yield point is not located at the contact area but is buried in the solid, and the deformation is restricted to EPL mode, as demonstrated by finite element simulation [12]. With the load increases, the plastic deformation increases and a fully plastic mode of deformation will eventually dominate at a certain load. In Fig. 4b and c, representative curves of $\sigma_{cont}$ and $\sigma_E$ against $\varepsilon_E$ for both TCPs are plotted. According to $\sigma_{cont}$-$\varepsilon_E$ data, all cases show a stress-stabilized stage in the EPL regime, but the $\sigma_{cont}$ will rise evidently during severe plastic deformation ($\varepsilon_E$>0.5). In $\sigma_E$-$\varepsilon_E$ curves, the maximum flow stress could achieve as high as ~8 and ~6 GPa for the smallest Ti-TiBw and Ti64-TiBw particles measured, respectively. This value is higher than some recent results for some single-crystalline submicron particles, such as Mo [12], Ni and Ni–50Fe [11], and Au [14], and several times higher than that of polycrystalline Au particles

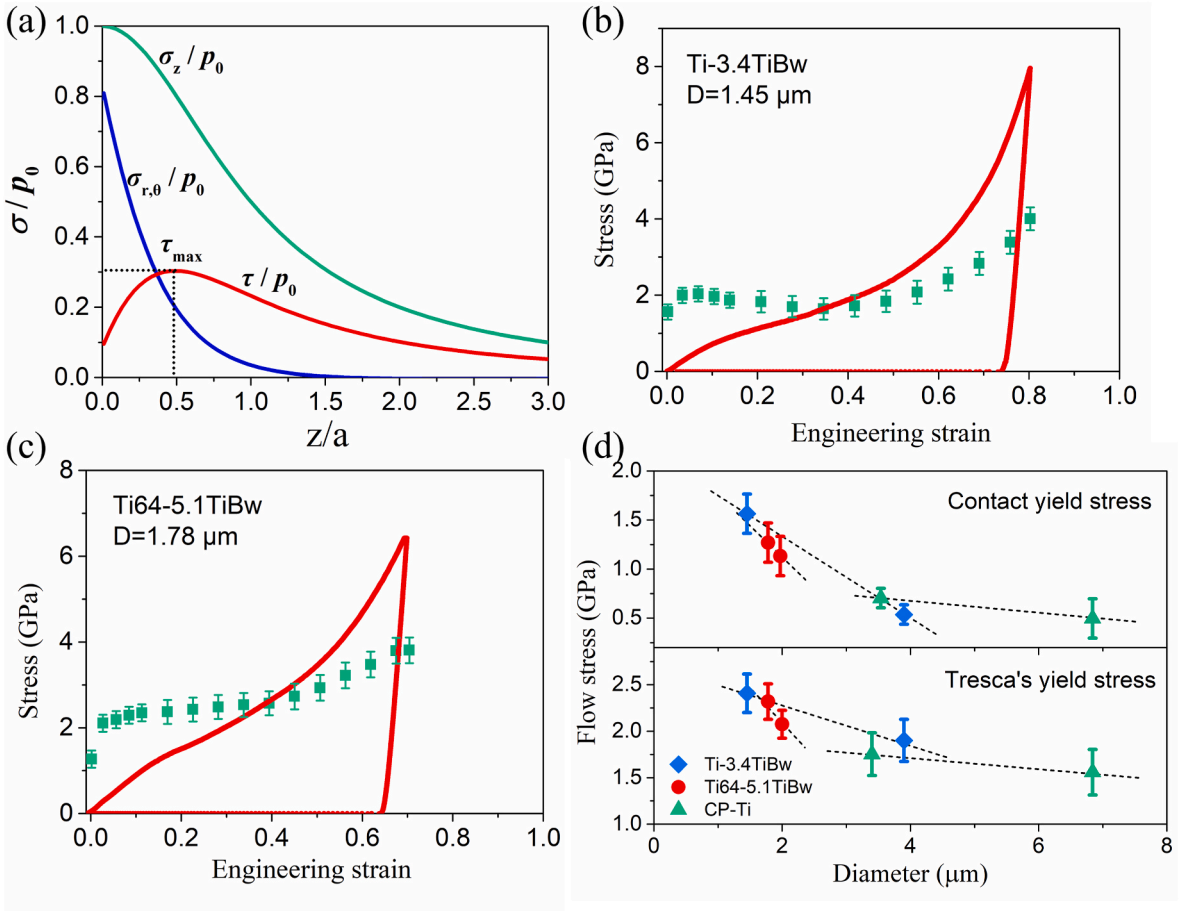


**Fig. 4.** Stress-strain relationship of TCPs. (a) Principal and shear stress distribution along the axis of revolution of a compressed TCP under Hertzian contact ($\nu$ = 0.32). The maximum shear stress locates on the axis of loading in a depth of z = ~0.5a with $\tau_{max} = 0.3p_0$. (b, c) Contact pressure (squares) and engineering stress (solid lines) as a function of engineering strain for the smallest Ti-TiBw and Ti64-TiBw particles. (d) Actual contact yield stress and calculated yield stress based on Tresca criterion as a function of diameter of Ti-TiBw, Ti64-TiBw and CP-Ti particles.

[13]. Compare with results of pillars, the $\sigma_{cy}$ at $\varepsilon_E = -0.2\%$ ($\sigma_{0.2}$) is taken as the engineering yield stress. For the reference CP-Ti particles, the $\sigma_{0.2}$ increases from 430 to 490 MPa with the diameter decrease from 5.2 to 3.5 μm. The increase of $\sigma_{0.2}$ is also observed for some TCPs. The $\sigma_{0.2}$ of the smallest Ti-TiBw ($D$~1.45 μm) and Ti64-TiBw ($D$~1.78 μm) particles could achieve as high as ~810 and ~1150 MPa. In some reports, the $\sigma_{cont}$ at the first strain burst is also regarded as the yield point [11,12,43]. As plotted in Fig. 4b and c, the first $\sigma_{cont}$ is usually higher than the $\sigma_E$ ($\sigma_{0.2}$) even we considered the experimental uncertainty carefully. According to the definition, the $\sigma_{0.2}$ is obviously underestimated because the elastic-plastic deformation only occurs in a small volume but the instantaneous load is divided by the whole projected area of a pristine particle. Thus, we regard the $\sigma_{cont}$ as the upper bound of yield strength, that is, for example, for the smallest Ti-TiBw and Ti64-TiBw particles, the $\sigma_{cy}$ at local area could achieve ~1.51 and ~1.29 GPa, respectively. In Fig. 4d, we found that the smaller particles have higher $\sigma_{cont}$, which also implies the increased hardness for smaller particles in the elastic-plastic regime [13,44].

## 4. Discussion

### 4.1. Deformation and failure in Ti64-TiBw particles

In a stark contrast to CP-Ti, flow instability and inhomogeneous deformation usually occurs in compressed bulk Ti64 alloy at elevated/room temperatures and/or high strain rates [45–48]. The catastrophic failure, even for ultrafine-grained (UFG) Ti64 with grains down to ~300 nm, is predominant by a combination of multiscale shear bands with shear dimples, regardless of equiaxed or Widmanstätten microstructures [47,48]. For bulk Ti64-TiBw composites, similar cracking failure is also observed in the inset in Fig. 2f as well as in literature [49]. When bulk Ti64 alloy decreases to micropillar with diameters less than 10 μm, multiple shear slips are observed as the main failure manner instead of macroscopic cracks, and the slip configuration depends on the phase and orientation [50]. However, good microscale plasticity, that is, neither the catastrophic cracking nor slip extrusion is found in compression of all tested Ti64-TiBw particles (see an example in Fig. 5). This phenomenon is also verified by the *F-h* curves of Ti64-TiBw particles that showing no discontinuity and load drop till severe plastic deformation. The failure of Ti64 alloy largely depends on its constituent phases and their morphology and characteristic length scales, as well as the size and orientation of prior-β grains. Ultrafine α+β structure which formed during rapid solidification process, e.g. nanosized α-laths prepared by additive manufacturing, usually retards the propagation of microcracks along the GBs of α-laths under uniaxial stresses [51,52]. More α/β interfaces and small α grains are considered to disperse load and resist fracture [52]. Thus, we suggest that fine grains in gas-atomized Ti64-TiBw particles also lead to similar effect, which is further stabilized by the pinning of nano-TiBw. The details of the microscale plasticity in Ti64-TiBw particles need further postmortem investigation of microstructures.

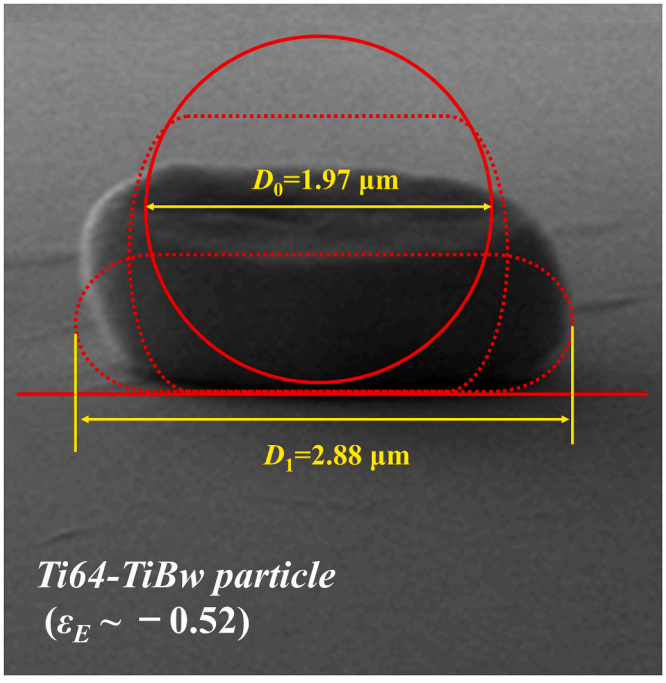


**Fig. 5.** Geometrical shape and surface morphology of a severely deformed Ti64-TiBw particle at compressive strain of $\varepsilon_E$ ~ -0.52.

### 4.2. Strain hardening of TCPs under compression

Although the strain hardening behavior in CP-Ti and Ti64 varies with the grain size, strain rate and temperature, a common feature that having only one increased strain hardening stage followed by a softening at the end is frequently reported [45,48,53–55]. In the present work, to quantify the global stain hardening of a single TCP after elastic-plastic deformation, a harmonic mean approximation in which a sphere is converted to a cylinder by assuming the constancy of volume is employed, and the equivalent stress $\sigma_{eq}$ and strain $\varepsilon_{eq}$ are given by Stauffer et al. [18]:

$$\sigma_{eq} = 2 / \left(\sigma_{sphere}^{-1} + \sigma_{cylinder}^{-1}\right) \quad (6)$$

$$\varepsilon_{eq} = 2 / \left(\varepsilon_{sphere}^{-1} + \varepsilon_{cylinder}^{-1}\right) \quad (7)$$

Here $\sigma_{sphere}$ and $\varepsilon_{sphere}$ are the contact pressure and Tabor strain for a compressed sphere and the subscripts are for the corresponding shapes. By analyzing the geometric evolution of a single TCP (see solid and dashed lines in Fig. 5), the equivalent cylinder approximation is reasonable for stressed TCPs at $\varepsilon_E$>-0.2. Then, the true stress ($\sigma_T$)-true strain ($\varepsilon_T$) relationship is found from $\sigma_T = \sigma_{eq}(1+\varepsilon_{eq})$ and $\varepsilon_T = \ln(1+\varepsilon_{eq})$, and the strain hardening exponents, $n$, is determined by the Hollomon equation, $\sigma_T = k\varepsilon_T^n$. Compared with bulk CP-Ti, Ti64 alloy and their composites, similar features of strain hardening are observed in these TCPs. This could be better seen based on the analysis in strain hardening rate ($\theta = d\sigma_T/d\varepsilon_T$) as shown in Fig. 6a and b. The $\theta$-increasing stage is located at small strains and the falling of $\theta$ is interpreted by dynamic recovery or easy glide in CP-Ti by different authors [45,54]. The increased $\theta$ value could achieve ~33.9 and ~37.4 GPa for the smallest Ti-TiBw and Ti64-TiBw particles, respectively. It is found that the deformation twins appears to reduce effective slip distance and increase the $\theta$ by Hall-Petch hardening mechanism at this stage [54]. The intermediate stage is a plateau of $\theta$ which exists in a wide strain range from −0.02 to −0.2. The underlying mechanism may be related to the competition between the dislocation nucleation (activation) rate and the mobile dislocation annihilation rate [50]. At higher plastic strains, enhanced friction between sample-indenter contacts and geometric shape effect lead to ultrahigh $\theta$ value. The strain hardening exponent $n$ in EPL mode is also calculated for both TCPs. The $n$ value for small-sized and bulk composites falls within a range of 0.5–0.7, which is consistent with the results of CP-Ti, Ti64 alloy and most metals [23,54,56].

### 4.3. Strengthening mechanism of TCPs

When dealing with small-sized metals, both the intrinsic (grain size $d$) and extrinsic size (sample size $D$) effects should be considered. The intrinsic size effect can be well predicted by the famous Hall-Petch relationship, while the extrinsic sample-size-dependent effect is usually understood by dislocation source-limitation mechanism [57,58].

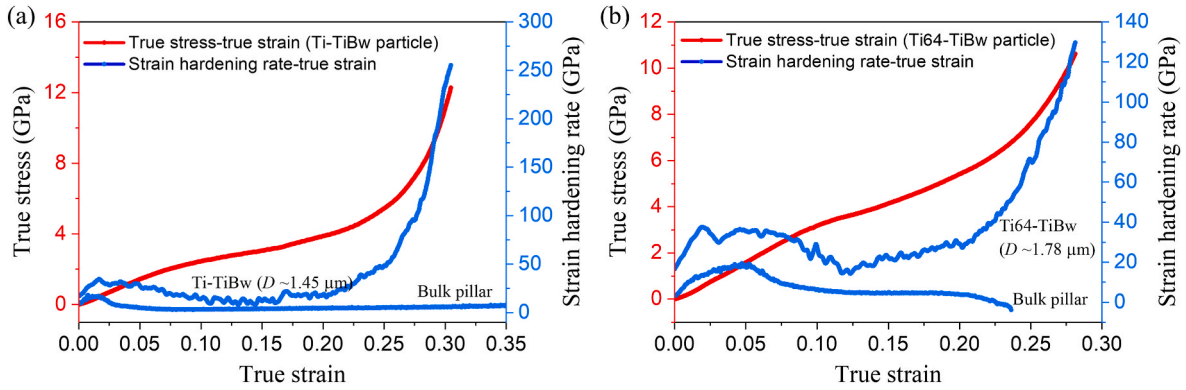


**Fig. 6.** Strain hardening behaviors of TCPs. True stress (strain hardening rate)-true strain curves of a single (a) Ti-TiBw and (b) Ti64-TiBw particle. The data for bulk composite pillars are also plotted for comparison.

For polycrystalline Ti, the strength contributed by the Hall-Petch mechanism depends on the grain size $d$ and the microstructure. As processed by equal channel angular pressing (ECAP), the $\sigma_{cy}$ of CP-Ti by reducing $d$ from 35 to 0.25 μm is merely enhanced from 500 to 560 MPa [59]. However, by ECAP plus cold rolling, the $\sigma_{cy}$ could significantly achieve as high as ~1000 MPa after a similar change of $d$, due to the formation of deformation twins [53]. For bimodal Ti64 alloy, the increased strength $\Delta\sigma_{cy}$ caused by grain refinement from 15 to 0.71 μm is ~430 MPa [60]. A micro-tensile study for Ti64 demonstrated that the equiaxed microstructure with $d$ from ~25 to 0.31 μm leads to $\Delta\sigma_y$~360 MPa, while two bimodal microstructures can be strengthened by $\Delta\sigma_y$ ~232 and ~204 MPa as the $d$ decreases in the range of ~25–0.69 μm [57]. On the other hand, the $D$-dependent effect was reported in small-sized CP-Ti and Ti64 alloy by Kishida et al. and R. Ameen, but it has not been observed by Tian et al. [21,50,61]. In Fig. 7, we compare our results for TCPs with some published results from bulk to microscale samples in $\sigma_{cy}$-$D$ scheme. Though the contact yield stress of TCPs is relatively higher than bulk results, it cannot safely conclude the D-dependent strengthening is valid for TCPs. For convenience, published results of compressive properties of TMCs and CP-Ti from bulk to microscale have been summarized in Table 1.

Besides abovementioned size effects, a portion of strengthening for the whisker/fiber/nanotube reinforced metallic matrix composites derives from the pinning effect or load transfer mechanism, which can be described by the classic shear-lag model [33,62,63]:

$$\sigma_y = \sigma_m\left(\frac{V_f S}{2}+1\right) \tag{8}$$

where the $\sigma_m$ and $V_f$ is the yield strength of matrix and the volume fraction of whiskers, respectively. For a given TCP, the average $S$ and $d$ can be statistically determined by SEM measurements. In our case, the $\sigma_{cy}$ of CP-Ti particle with $d$~0.25 μm achieves ~704 MPa. By Eq. (8), the yield strength of TCPs should be predicted by a combined contributions from Hall-Petch strengthening and the load-transfer effect. Taking above parameters for Ti-TiBw particles into consideration, the $S = 42$, $V_f = 3.4\%$, $d = 0.25$ μm, $\sigma_m = 704$ MPa, yields the calculated $\sigma_{cy}$ to be ~1206 for the smallest TCP. This calculated result falls within the upper and lower bounds of yield stress for Ti-TiBw particles.

In Fig. 8, we interpret the strengthening and strain hardening of TCPs in terms of the architecture of nano-TiBw network. It is known that dislocation movement can be impeded by the presence of GBs. The way in which dislocations pass through these GBs and move into neighboring grains has an effect on the numbers of dislocations within a grain and the force required to move them. In our cases, the reinforcement network that distributed along the GBs acts as a stronger barrier to pin dislocation motion. Let us consider a grain closely embraced by nano-TiBw, a shear stress is acting on a slip system with a sufficiency of mobile dislocations. At first, dislocations will easily move along the slip plane until they reach the stiff nano-TiBw network, where they are blocked, and will further pileup due to the barriers generated by the lattice mismatch between two adjacent grains upon plastic deformation. In the second stage, the internal grains are capable of holding more dislocation pileups, leading to a higher driving force for dislocation movement to adjacent grains. At last, a combination effect of the dislocation pileups inside internal grains, stress concentration near the nano-TiBw networks, will contribute the enhanced strain hardening in EPL regime.

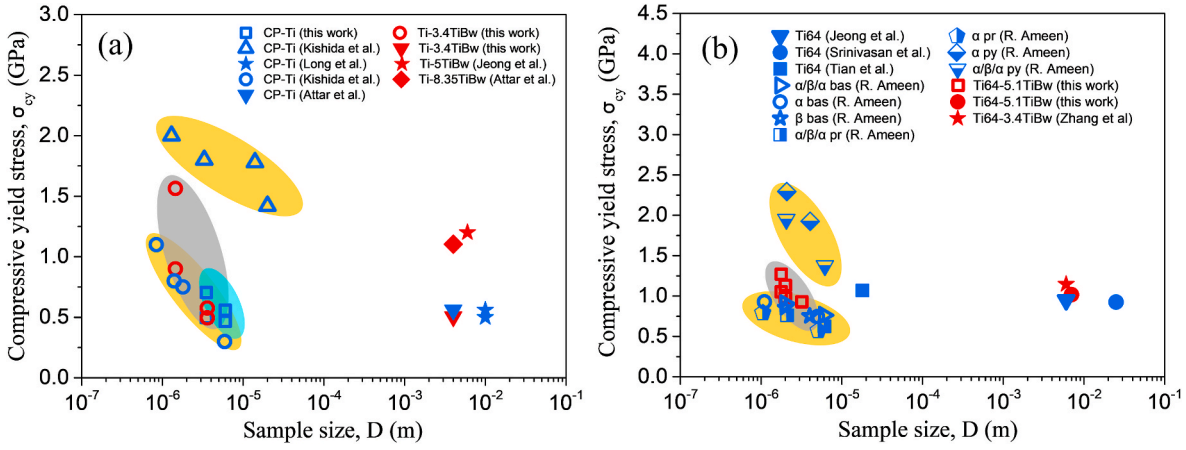


**Fig. 7.** Compressive yield strength of (a) CP-Ti and Ti-TiBw composites, and (b) Ti64 alloy and Ti64-TiBw composites from bulk to small scales.

**Table 1**
Compressive properties of TMCs, CP-Ti and Ti64 at different length scales.

| Materials | Methods | Specimen type & size/μm | Yield Strength/MPa | Max. flow stress/MPa | Max. strain/% | Fracture | Ref. |
|---|---|---|---|---|---|---|---|
| **CP-Ti** | EIGA | Particle, *D* ~3 | ~704 | ~1630 | ~54.6 | No | This work |
| **Ti-3.4 vol% TiBw** | EIGA | Particle, *D* ~1.4 | ~1563 | ~7931 | ~80.1 | No | This work |
| **Ti64-5.1 vol% TiBw** | EIGA | Particle, *D* ~1.8 | ~1269 | ~6418 | ~69.6 | No | This work |
| **Ti-3.4 vol% TiBw** | SPS | Pillar, *D* ~4000, *H* ~6000 | ~505 | ~1670 | ~46.2 | No | This work |
| **Ti64-5.1 vol% TiBw** | SPS | Pillar, *D* ~7000, *H* ~7000 | ~1058 | ~1600 | ~27.5 | Yes | This work |
| **CP-Ti** | Arc melting | Micropillar, *L* ~0.84-30 | [0001] ~1450-2000<br>[2-1-10] ~300-1100 | [0001] ~2200-2800<br>[2-1-10] ~400-1300 | [0001] 5<br>[2-1-10] 10 | No | [21] |
| **Ti-8.35 vol% TiBw** | SLM | Pillar | ~1103 | ~1421 | ~17.8 | Yes | [64] |
| **CP-Ti** | SLM | Pillar | ~560 | ~1136 | ~52 | No | [64] |
| **Ti-5 vol% TiBw** | Powder metallurgy | Pillar, *D* ~6000, *H* ~9000 | ~1200 | ~1420 | ~8.5 | Unknown | [65] |
| **Ti-10 vol% TiBw** | Powder metallurgy | Pillar, *D* ~6000, *H* ~9000 | ~1400 | ~1650 | ~5.5 | Unknown | [65] |
| **Ti-20 vol% TiBw** | Powder metallurgy | Pillar, *D* ~6000, *H* ~9000 | ~1650 | ~1740 | ~2.8 | Unknown | [65] |
| **Ti64** | Unknown | Pillar, *D* ~6000, *H* ~9000 | ~950 | ~1080 | ~8 | Unknown | [65] |
| **Ti64** | EBM | Pillar, *D* ~18, *H* ~40 | 860–1070 | 1400–1750 | ~17.5 | No | [61] |
| **Ti64** | HT | Pillar, *D* 1-6 | α/β/α, 763-905<br>single α, 745-928<br>single β, 752-854 | ~900–1400<br>~1010–1340<br>~1120–1490 | ~4–9<br>~5.7–7.6<br>~5–7 | No | [50] |
| **CP-Ti** | SLM | Pillar, *D* ~4000, *H* ~10,000 | – | ~1136 | ~51 | Unknown | [66] |
| **CP-Ti** | ECAP | Square pillar, L, W, H>10,000 | CG, ~500<br>UFG, ~560 | CG, ~820<br>UFG, ~900 | CG, ~60<br>UFG, ~35 | No<br>No | [59] |
| **Ti64** | Annealed | Rod, *D* ~25,000, *H* ~37,500 | ~925 | ~1300 | ~10 | No | [67] |
| **Ti64-TiBw** | SLM | Pillar, *D* ~6000, *H* ~8000 | ~1147 | ~1680 | ~20.1 | Yes | [68] |

Note: *D*, *H*, *W* and *L* indicates diameter, height, width and edge length of samples, respectively.
EIGA: Electrode induction melting gas atomization.
SPS: Spark plasma sintering.
EBM: Electron beam melting.
HT: Heat treatment.
SLM: Selective laser melting.
ECAP: Equal channel angular pressing.
CG/UFG: Coarse-/Ultrafine-grained.

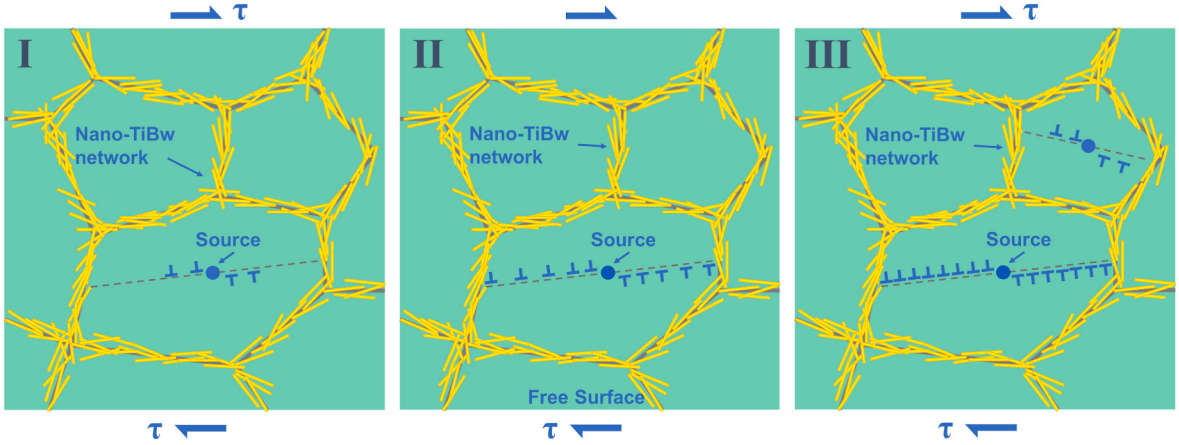


**Fig. 8.** Schematic of deformation mechanism for TCPs.

## 5. Conclusions

In summary, this study presents an experimental investigation of elastic and plastic behaviors of two common TCPs with diameter of 1–5 μm under uniaxial compression. According to the analysis in Hertzian contact, the effective reduced Young's modulus for Ti-TiBw and Ti64-TiBw particles is estimated to be ~85 and ~95 GPa, respectively. In elastic-plastic regime, flow stresses in both TCPs exceed that in bulk composite pillars. The contact yield stress for Ti-TiBw and Ti64-TiBw particles fall within ~0.5–1.5 GPa and ~1.1–1.3 GPa, which the value increases with the particle size decreases. Good microscale plasticity is found in Ti64-TiBw particles during large deformation, rather than catastrophic cracking in bulk composite. The reason may stem from more α/β interfaces and small α grains in gas-atomized Ti64-TiBw particles which are beneficial to disperse load and resist fracture. Compared with bulk composites, enhanced strain hardening is observed by a manifestation of high strain hardening rate of ~34.2 and ~37.5 GPa for Ti-TiBw and Ti64-TiBw particles in EPL regime, indicating the significant role of nano-TiBw network in pinning dislocation and GBs, and resisting shear deformation.

This work may stimulate the exploration of the micromechanical behaviors and properties of various metallic matrix composites at small-sized scales by the virtue of MCPs.

## CRediT authorship contribution statement

**Bo Li:** Investigation, Conceptualization, Methodology, Formal analysis, Data curation, Writing – original draft. **Deng Pan:** Investigation, Methodology, Data curation. **Xin Zhang:** Investigation, Data curation. **Lei Liu:** Investigation, Methodology, Data curation. **Lina Gao:** Methodology. **Shaolong Li:** Methodology. **Yuanbin Qin:** Methodology. **Yabo Fu:** Investigation, Conceptualization, Methodology. **Shufeng Li:**

Methodology, Funding acquisition, Conceptualization, Project administration.

## Declaration of competing interest

The authors declare that they have no known competing financial interests or personal relationships that could have appeared to influence the work reported in this paper.

## Data availability

Data will be made available on request.

## Acknowledgements

The authors acknowledge the financial support of National Key Research and Development Program of China (No. 2021YFB3701203), Shaanxi Innovative Research Team for Key Science and Technology (No. 2023-CX-TD-46), and Zhejiang Provincial Natural Science Foundation of China (No. LGG20E010004). B. Li is personally supported by Natural Science Basic Research Program of Shaanxi (No. 2023-JC-YB-420), Doctoral Teacher Starting Fund of Xi'an University of Technology (No. 101–451121008) and the Open Fund of Zhejiang Provincial Key Laboratory for Cutting Tools (No. ZD202102). X. Zhang is personally supported by National Natural Science Foundation of China (No. 52201165), Guangdong Basic and Applied Basic Research Foundation (No. 2021A151511116) and Doctoral Teacher Starting Fund of Xi'an University Technology (No. 101-451121007).

## References

[1] L. Liu, S.F. Li, D. Pan, D.X. Hui, X. Zhang, B. Li, T.S. Liang, P.P. Shi, A. Bahador, J. Umeda, K. Kondoh, S.L. Li, L.N. Gao, Z.M. Wang, G. Li, S.Y. Zhang, R.H. Wang, W.G. Chen, Loss-free tensile ductility of dual-structure titanium composites via interdiffusion and self-organization strategy, Proc. Natl. Acad. Sci. USA 120 (2023), e2302234120.

[2] D. Pan, S. Li, L. Liu, X. Zhang, B. Li, B. Chen, M. Chu, X. Hou, Z. Sun, J. Umeda, K. Kondoh, Enhanced strength and ductility of nano-TiBw-reinforced titanium matrix composites fabricated by electron beam powder bed fusion using Ti6Al4V–TiBw composite powder, Addit. Manuf. 50 (2022), 102519.

[3] D. Pan, X. Zhang, X. Hou, Y. Han, M. Chu, B. Chen, L. Jia, K. Kondoh, S. Li, TiB nano-whiskers reinforced titanium matrix composites with novel nano-reticulated microstructure and high performance via composite powder by selective laser melting, Mater. Sci. Eng., A 799 (2021), 140137.

[4] S. Li, X. Wang, Z. Wei, Y. Han, H. Shi, J. Le, G. Huang, D. Zhang, W. Lu, Simultaneously improving the strength and ductility of the as-sintered (TiB+ La2O3)/Ti composites by in-situ planting ultra-fine networks into the composite powder, Scripta Mater. 218 (2022), 114835.

[5] S. Li, Y. Han, X. Wang, G. Huang, M. Fang, H. Shi, J. Le, W. Lu, Novel strategy of planting nano-TiB fibers with ultra-fine network distribution into Ti-composite powder and its thermal transition mechanism, Compos. Commun. 29 (2022), 101002.

[6] M. Chen, X. Li, G. Ji, Y. Wu, Z. Chen, W. Baekelant, K. Vanmeensel, H. Wang, J. P. Kruth, Novel composite powders with uniform TiB2 nano-particle distribution for 3D printing, Appl. Sci. 7 (2017) 250.

[7] X.P. Li, G. Ji, Z. Chen, A. Addad, Y. Wu, H.W. Wang, J. Vleugels, J. Van Humbeeck, J.P. Kruth, Selective laser melting of nano-TiB2 decorated AlSi10Mg alloy with high fracture strength and ductility, Acta Mater. 129 (2017) 183–193.

[8] C. Dan, Y. Cui, Y. Wu, Z. Chen, H. Liu, G. Ji, Y. Xiao, H. Chen, M. Wang, J. Liu, L. Wang, Y. Li, A. Addad, Y. Zhou, S. Ma, Q. Shi, H. Wang, J. Lu, Achieving ultrahigh fatigue resistance in AlSi10Mg alloy by additive manufacturing, Nat. Mater. 22 (2023) 1182–1188.

[9] H. Shi, Y. Zhao, H. Gao, M. Zhang, Y. Jiang, F. Cao, J. Zou, S. Liang, In-situ spherical TiB2/Cu composite powder: a new method of liquid phase reaction coupled with gas atomization, Mater. Char. 191 (2022), 112096.

[10] M. Chaudhri, I. Hutchings, P. Makin, Plastic compression of spheres, Philos. Mag. A 49 (1984) 493–503.

[11] A. Sharma, O. Mendelsohn, A. Bisht, J. Michler, R.K. Koju, Y. Mishin, E. Rabkin, Solid-solution and precipitation softening effects in defect-free faceted Nickel-Iron nanoparticles, Acta Mater. 243 (2023), 118527.

[12] A. Sharma, R. Kositski, O. Kovalenko, D. Mordehai, E. Rabkin, Giant shape- and size-dependent compressive strength of molybdenum nano- and microparticles, Acta Mater. 198 (2020) 72–84.

[13] J. Paul, S. Romeis, P. Herre, W. Peukert, Deformation behavior of micron-sized polycrystalline gold particles studied by in situ compression experiments and frictional finite element simulation, Powder Technol. 286 (2015) 706–715.

[14] D. Mordehai, S.W. Lee, B. Backes, D.J. Srolovitz, W.D. Nix, E. Rabkin, Size effect in compression of single-crystal gold microparticles, Acta Mater. 59 (2011) 5202–5215.

[15] J. Paul, S. Romeis, J. Tomas, W. Peukert, A review of models for single particle compression and their application to silica microspheres, Adv. Powder Technol. 25 (2014) 136–153.

[16] K. Zheng, C. Wang, Y.Q. Cheng, Y. Yue, X. Han, Z. Zhang, Z.W. Shan, S. Mao, M. Ye, Y. Yin, E. Ma, Electron-beam-assisted superplastic shaping of nanoscale amorphous silica, Nat. Commun. 1 (24) (2010) 1–8.

[17] B. Li, Y. Nan, X. Zhao, P. Zhang, X. Song, Graphene-size-tuned mechanical serration behaviors in nanocarbons, Acta Mater. 162 (2019) 116–125.

[18] D. Stauffer, A. Beaber, A. Wagner, O. Ugurlu, J. Nowak, K. Andre Mkhoyan, S. Girshick, W. Gerberich, Strain-hardening in submicron silicon pillars and spheres, Acta Mater. 60 (2012) 2471–2478.

[19] J. He, Z. Zhang, M. Midttun, G. Fonnum, G. Modahl, H. Kristiansen, K. Redford, Size effect on mechanical properties of micron-sized PS–DVB polymer particles, Polymer 49 (2008) 3993–3999.

[20] J. Greer, J. De Hosson, Plasticity in small-sized metallic systems: intrinsic versus extrinsic size effect, Prog. Mater. Sci. 56 (2011) 654–724.

[21] K. Kishida, J.G. Kim, T. Nagae, H. Inui, Experimental evaluation of critical resolved shear stress for the first-order pyramidal c + a slip in commercially pure Ti by micropillar compression method, Acta Mater. 196 (2020) 168–174.

[22] K. Eswar Prasad, K. Rajesh, U. Ramamurty, Micropillar and macropillar compression responses of magnesium single crystals oriented for single slip or extension twinning, Acta Mater. 65 (2014) 316–325.

[23] S. Lei, J.Y. Zhang, J.J. Niu, G. Liu, X. Zhang, J. Sun, Intrinsic size-controlled strain hardening behavior of nanolayered Cu/Zr micropillars, Scripta Mater. 66 (2012) 706–709.

[24] S.W. Lee, W.D. Nix, Size dependence of the yield strength of fcc and bcc metallic micropillars with diameters of a few micrometers, Philos. Mag. A 92 (2012) 1238–1260.

[25] B. Li, C. Hu, K. Shi, D. Pan, X. Zhang, L. Liu, L. Gao, S. Li, Z. Wang, G. Li, Y. Fu, L. Su, S. Li, Pressure-driven structural transformation and lattice deformation in TiB reinforced titanium matrix composites: an in-situ synchrotron x-ray diffraction study, Mater. Charact. (2023).

[26] M. Hayat, H. Singh, Z. He, P. Cao, Titanium metal matrix composites: an overview, Composites Part A 121 (2019) 418–438.

[27] G. Singh, U. Ramamurty, Boron modified titanium alloys, Prog. Mater. Sci. 111 (2020), 100653.

[28] N. Liu, X. Zhang, Q. Zhang, Y. Jiang, Y. Su, Q. Li, P. Feng, W. Tang, S. Liang, Numerical evaluation and experimental verification of mechanical properties and fracture behavior for TiB2/Cu composites prepared by in-situ mixing casting, J. Alloys Compd. 895 (2022), 162475.

[29] N. Liu, Q. Zhang, H. Zhang, F. Cao, P. Feng, Y. Zuo, Y. Jiang, W. Tang, S. Liang, Experimental verification and numerical analysis on plastic deformation and mechanical properties of the in-situ TiB2 homogeneous composites and TiB2/Cu network composites prepared by powder metallurgy, J. Alloys Compd. 920 (2022), 165897.

[30] N. Liu, Q. Zhang, P. Feng, Y. Zuo, F. Han, Y. Xu, Y. Jiang, W. Tang, S. Liang, Effects of configuration parameters on the deformation and fracture behaviors of TiB2/Cu composites with network structure: a numerical approach using an enhanced finite element model, Comput. Mater. Sci. 205 (2022), 111212.

[31] N. Liu, X. Zhang, X. Zhang, P. Feng, Y. Zuo, F. Cao, Y. Su, Y. Jiang, S. Liang, Numerical investigations on the hybrid effect and deformation mechanism of TiB2p and TiBw reinforced Cu composites prepared by in-situ mixing casting, Comput. Mater. Sci. 213 (2022), 111657.

[32] H. Feng, Y. Zhou, D. Jia, Q. Meng, J. Rao, Growth mechanism of in situ TiB whiskers in spark plasma sintered TiB/Ti metal matrix composites, Cryst. Growth Des. 6 (2006) 1626–1630.

[33] M.K. Koo, J.S. Park, M.K. Park, K.T. Kim, S.H. Hong, Effect of aspect ratios of in situ formed TiB whiskers on the mechanical properties of TiBw/Ti-6Al-4V composites, Scripta Mater. 66 (2012) 487–490.

[34] N. Liu, Q. Li, Y. Jiang, Y. Su, W. Tang, S. Liang, Composite structural modeling and mechanical behavior of whisker reinforced Cu matrix composites, Comput. Mater. Sci. 195 (2021), 110492.

[35] L. Huang, Q. An, L. Geng, S. Wang, S. Jiang, X. Cui, R. Zhang, F. Sun, Y. Jiao, X. Chen, C. Wang, Multiscale architecture and superior high-temperature performance of discontinuously reinforced titanium matrix composites, Adv. Mater. 33 (2020), 2000688.

[36] H. Feng, Y. Zhou, D. Jia, Q. Meng, Stacking faults formation mechanism of in situ synthesized TiB whiskers, Scripta Mater. 55 (2006) 667–670.

[37] H. Feng, Y. Zhou, D. Jia, Q. Meng, Rapid synthesis of Ti alloy with B addition by spark plasma sintering, Mater. Sci. Eng., A 390 (2005) 344–349.

[38] C.A. Klein, G.F. Cardinale, Young's modulus and Poisson's ratio of CVD diamond, Diam. Relat. Mater. 2 (1993) 918–923.

[39] M.A. Hopcroft, W.D. Nix, T.W. Kenny, What is the Young's modulus of silicon? J. Microelectromech. Syst. 19 (2010) 229–238.

[40] L.J. Huang, L. Geng, Discontinuously Reinforced Titanium Matrix Composites, National Defense Industry Press, Beijing and Springer Nature Singapore Pte Ltd, 2017.

[41] Z. Hashin, S. Shtrikman, A variational approach to the theory of the elastic behaviour of multiphase materials, J. Mech. Phys. Solid. 11 (1963) 127–140.

[42] T.W. Clyne, P.J. Withers, An Introduction to Metal Matrix Composites, Cambridge University Press, UK, 1993.

[43] Z.J. Wang, Z.W. Shan, J. Li, J. Sun, E. Ma, Pristine-to-pristine regime of plastic deformation in submicron-sized single crystal gold particles, Acta Mater. 60 (2012) 1368–1377.
[44] D. Tabor, The Hardness of Metals, Oxford University Press, 2000.
[45] S. Kailas, Y. Prasad, S. Biswas, Flow instabilities and fracture in Ti6-6Al-4V deformed in compression at 298 K to 673 K, Metall. Mater. Trans. A 25A (1994) 2173–2179.
[46] A. Wagoner Johnson, C. Bull, K. Kumar, C. Briant, The influence of microstructure and strain rate on the compressive deformation behavior of Ti-6Al-4V, Metall. Mater. Trans. A 34A (2003) 295–306.
[47] Y. Long, L. Peng, W. Zhang, H. Peng, J. Zhang, X. Huang, Effect of grain size on the shear banding behavior of Ti-6Al-4V alloy under quasi-static compression, Metall. Mater. Trans. A 51 (2020) 2064–2071.
[48] Y. Long, W. Zhang, L. Peng, H. Peng, X. Li, X. Huang, Mechanical behaviors of ultrafine-grained Ti-6Al-4V alloy during compression at various strain rates, Metall. Mater. Trans. A 51 (2020) 4765–4776.
[49] H. Li, D. Jia, Z. Yang, X. Liao, H. Jin, D. Cai, Y. Zhou, Effect of heat treatment on microstructure evolution and mechanical properties of selective laser melted Ti–6Al–4V and TiB/Ti–6Al–4V composite: a comparative study, Mater. Sci. Eng., A 801 (2021), 140415.
[50] R.B.M. Ameen, Plastic Deformation of Ti-6Al-4V at Small Scale: a Microstructural and Mechanistic Study, University of Birmingham, UK, 2017.
[51] W. Xu, M. Brandt, S. Sun, J. Elambasseril, Q. Liu, K. Latham, K. Xia, M. Qian, Additive manufacturing of strong and ductile Ti–6Al–4V by selective laser melting via in situ martensite decomposition, Acta Mater. 85 (2015) 74–84.
[52] Y. Ren, X. Lin, X. Fu, H. Tan, J. Chen, W.D. Huang, Microstructure and deformation behavior of Ti-6Al-4V alloy by high-power laser solid forming, Acta Mater. 132 (2017) 82–95.
[53] Y.M. Wang, J.Y. Huang, T. Jiao, Y.T. Zhu, A.V. Hamza, Abnormal strain hardening in nanostructured titanium at high strain rates and large strains, J. Mater. Sci. 42 (2007) 1751–1756.
[54] A.A. Salem, S.R. Kalidindi, R.D. Doherty, Strain hardening regimes and microstructure evolution during large strain compression of high purity titanium, Scripta Mater. 46 (2002) 419–423.
[55] S. Nemat-Nasser, W. Guo, J. Cheng, Mechanical properties and deformation mechanisms of a commercially pure titanium, Acta Mater. 47 (1999) 3705–3720.
[56] R. Gupta, V. Anil Kumar, C. Mathew, G. Sudarshan Rao, Strain hardening of Titanium alloy Ti6Al4V sheets with prior heat treatment and cold working, Mater. Sci. Eng., A 662 (2016) 537–550.
[57] Y. Chong, G. Deng, S. Gao, J. Yi, A. Shibata, N. Tsuji, Yielding nature and Hall-Petch relationships in Ti-6Al-4V alloy with fully equiaxed and bimodal microstructures, Scripta Mater. 172 (2019) 77–82.
[58] T.A. Parthasarathy, S.I. Rao, D.M. Dimiduk, M.D. Uchic, D.R. Trinkle, Contribution to size effect of yield strength from the stochastics of dislocation source lengths in finite samples, Scripta Mater. 56 (2007) 313–316.
[59] F.W. Long, Q.W. Jiang, L. Xiao, X.W. Li, Compressive deformation behaviors of Coarse- and ultrafine-grained pure titanium at different temperatures: a comparative study, Mater. Trans. 52 (2011) 1617–1622.
[60] Y. Long, H. Zhang, T. Wang, X. Huang, Y. Li, J. Wu, H. Chen, High-strength Ti-6Al-4V with ultrafine-grained structure fabricated by high energy ball milling and spark plasma sintering, Mater. Sci. Eng., A 585 (2013) 408–414.
[61] J. Tian, J. Ma, M. Yan, Z. Chen, J. Shen, J. Wu, Orientation dependence of the micro-pillar compression strength in an electron beam melted Ti–6Al–4V alloy, Acta Metall. Sin. 34 (2021) 476–484.
[62] H.J. Ryu, S.I. Cha, S.H. Hong, Generalized shear-lag model for load transfer in SiC/Al metal-matrix composites, J. Mater. Res. 18 (2003) 2851.
[63] W. Baxter, The strength of metal matrix composites reinforced with randomly oriented discontinuous fibers, Metall. Trans. A 23A (1992) 3045.
[64] H. Attar, M. Bönisch, M. Calin, L.C. Zhang, S. Scudino, J. Eckert, Selective laser melting of in situ titanium–titanium boride composites: processing, microstructure and mechanical properties, Acta Mater. 76 (2014) 13–22.
[65] H. Jeong, S. Kim, Y. Hyun, Y. Lee, Densification and compressive strength ofin-situ processed Ti/TiB composites by powder metallurgy, Met. Mater. Int. 8 (2002) 25–35.
[66] H. Attar, M. Calin, L. Zhang, S. Scudino, J. Eckert, Manufacture by selective laser melting and mechanical behavior of commercially pure titanium, Mater. Sci. Eng., A 593 (2014) 170–177.
[67] K. Srinivasan, P. Venugopal, Compression testing of Ti-6Al-4V in the temperature range of 303–873 K, Mater. Manuf. Process. 23 (2008) 342–346.
[68] J. Zhang, B. Song, C. Cai, L. Zhang, Y. Shi, Tailorable microstructure and mechanical properties of selective laser melted TiB/Ti–6Al–4V composite by heat treatment, Advanced Powder Materials 1 (2022), 100010.